EXPERIMENTAL INVESTIGATION OF THE VORTEX RING STATE FOR SIDE-BY-SIDE TANDEM PROPELLERS

Caterina Saglio, Daniele Granata, Alberto Savino and Alex Zanotti
Politecnico di Milano, Dipartimento di Scienze e Tecnologie Aerospaziali
via La Masa 34, 20156, Milan, Italy

ABSTRACT

The present paper describes an experimental wind tunnel campaign aimed at investigating the aerodynamic interactions between two side-by-side eVTOL propeller models in vortex ring state conditions. Load measurements and Particle Image Velocimetry (PIV) were employed in the comprehensive test campaign considering several configurations with different lateral distance between the propellers in side-by-side configuration, i.e. with aligned propeller disks, in both co-rotating and counter-rotating configurations. Tests results enabled to characterise the influence of the mutual aerodynamic influence between the two side-by-side propellers, providing insight into the loss of performance occurring on the propellers when entering in such descent flight condition. Moreover, PIV measurements enabled to get a detailed characterization of the velocity flow field and the vortical structures dimensions associated with vortex ring state occurrence in the different configurations tested.

NOTATION

C_T = thrust coefficient $= T/(\rho\pi R^4 n^2)$ [-]
C_T = thrust coefficient in hover [-]
C_Q = torque coefficient $= Q/(\rho\pi R^5 n^3)$ [-]
DR = descent ratio = V_∞/v_h
D_y = lateral distance between propellers
n = rotational speed [rad/s]
Q = propeller power [N m]
R = vortex radius [m]
R = propeller radius [m]
T = propeller thrust [N]
T_h = propeller thrust in hover [N]
V_h = rotor induced velocity = $\sqrt{T_h/(2\rho\pi R^2)}$
V_x = axial velocity component [m s^{-1}]
ρ = freestream air density [kg m^{-3}]

INTRODUCTION

One of the most critical aerodynamic conditions concerning safety for rotorcraft occurs during the vertical descent phase, i.e. vortex ring state (VRS). VRS is an aerodynamic condition that occurs when a rotor or propeller descends into its own wake, causing the airflow to recirculate around the rotor disk in the form of a vortex ring. This leads to a significant loss of thrust, generally resulting in reduced control and performance (Refs. 1,2). This phenomenon has been extensively investigated for rotors, particularly with application to helicopters or tiltrotors (Refs. 3–6). Although the phenomenon of vortex ring state has been extensively studied in conventional single-rotor configurations, as highlighted by Brown (Ref. 7), the development of new rotorcraft configurations in urban air mobility such as eVTOLs introduces new challenges. In fact, the combination of compact geometries, relatively low weight and high disc loading broadens the flight envelope in which VRS may occur. eVTOL designs often have features that increase sensitivity to VRS, such as small rotors, high blade twist and lateral rotor arrangements. Moreover, distinctive characteristics such as rpm control, lift generation from wings, multirotor aerodynamic interactions and thrust vectoring further differentiate eVTOLs from conventional rotorcraft and justify a revaluation of VRS susceptibility. To address these differences, some studies have investigated the VRS behavior in eVTOL configurations employing different methods. A recent contribution by Jeong et al. (Ref. 8) exemplifies this effort. In this work, a helicopter-based engineering model was extended to capture the effects of blade geometry and descent trajectories on VRS onset in eVTOLs. This adapted model allows for comparison of VRS susceptibility across different aircraft configurations and flight profiles. In particular, the obtained results suggest that the relatively low aerodynamic drag found in certain eVTOL configurations may increase susceptibility to VRS. This reinforces the need to further investigation into how eVTOL design features influence VRS onset and progression. Moreover, a ery recent contribution to the study of VRS for a real eVTOL propeller geometry is provided by Savino et al. (Ref. 9) describing results of a collaboration between Politecnico di Milano and Archer Aviation aimed at investigating by wind tunnel tests the occurrence and correlated flow physics of this phenomenon applied to the scaled geometry of the Archer Maker tilter propeller.

Despite increasing attention to this issue, the literature still lacks comprehensive and structured studies directly addressing VRS in multirotor configurations, resembling a more realistic configuration for an eVTOL aircraft and mainly limited to flow field evaluations (Ref. 10). However, the growing body of research on rotor-rotor aerodynamic interactions (Refs. 11, 12) reflects the increasing recognition of its relevance and urgency. Among the various aerodynamic phenomena affecting eVTOL performance, rotor–rotor interactions play a central role, especially due to the typical multirotor configurations used in these vehicles, where close spacing between propellers makes aerodynamic interference inevitable. As this type of aircraft often feature multiple propellers placed close together, the side-by-side configuration is a typical example. Due to the potential for aerodynamic interference, this setup has gained increasing attention in recent research. When propellers are closely spaced, they can experience significant wake interactions, which may lead to performance loss, unsteady aerodynamic loads, and even early onset of VRS. These challenges highlight the need for focused studies on rotor interactions in eVTOL designs.

The present paper is aimed to reduce this gap in literature by describing the results of an experimental study based on a comprehensive wind tunnel campaign on two side-by-side eVTOL propeller models in VRS conditions. Load measurements and Particle Image Velocimetry (PIV) were used to quantify aerodynamic performance variation and to investigate the flow physics around the propellers area for a dual-propeller system. In particular, in order to characterise VRS phenomenon for architectures typical of eVTOL aircraft, wind tunnel tests included configurations with different lateral distance between the propellers in side-by-side configuration, i.e. with aligned propeller disks, in both co-rotating and counter-rotating configurations. The aim of the tests was to characterise the mutual aerodynamic influence between the two side-by-side propellers, providing insight into the loss of performance occurring on the propellers when entering in such condition. Moreover, flow field surveys were performed to get a detailed characterization of the velocity field and the vortical structures associated with VRS phenomenon in the different configurations tested, as well as propeller wakes interactions. Finally, the comprehensive test campaign was aimed to collect an experimental data base, obtained over a free geometry, to be used for a robust validation of numerical models with different levels of fidelity, widely used for an effective and safe design of novel eVTOL architectures.

EXPERIMENTAL SET UP

The experimental campaign was conducted at the S. De Ponte wind tunnel, a closed-loop facility at the Aerodynamic Laboratory of the Department of Aerospace and Science Technology (DAER) of Politecnico di Milano, characterised by a 1.5m x 1 m test section with a maximum velocity of 55 m/s and a turbulence level below 0.1%. The experimental setup was characterized by two scaled models of eVTOL propellers (Ref. 12) equipped with three-bladed VarioProp 12C propellers, each with a nominal diameter of 300 mm (Ref. 12). The blades, made of a hobby-grade composite material, are attached to a central hub that allows for simultaneous adjustment of their collective pitch angle. Each hub is coupled with a 65 mm diameter aluminum spinner, designed to streamline the airflow around the root region and minimize undesired aerodynamic disturbances in the hub zone. The propeller system is driven by a Scorpion HKII-4235-630KV brushless electric motor, offering a continuous power output of 5.3 kW. The motor is powered and regulated through a PWM-controlled ESC (Scorpion Tribunus II 06-120A SBEC). The rotor hubs are equipped with a Hall-effect sensor positioned beneath the motor assembly to provide one signal per revolution for both rotational speed monitoring and phase-locked synchronization of PIV measurements. Rotational speed is regulated using a custom LabVIEW-based control system, which also handles data acquisition. Due to hardware limitations in the available hobby-grade ECS system, the blade azimuth phase of the propellers was not synchronized. However, the phase offset was considered negligible for the objectives of the experimental campaign. The motor, hub and instrumentation of each propeller are housed within a custom-made polycarbonate nacelle of 270 mm length, manufactured using Fused Deposition Modeling 3D printing. An internal aluminum support frame ensures rigid mounting and correct load transmission to a bi-axial strain gauge balance, allowing for accurate aerodynamic force measurements. The propeller configuration was tailored to reproduce descent flight conditions. Therefore, the propellers were mounted so that the wind tunnel flow impinged them from below, simulating the relative flow direction during vertical descent. The propellers were mounted vertically aligned, on a metallic frame built from Bosch aluminum profiles. This frame was designated to allow vertical translation of one propeller, enabling precise control of the tip-to-tip distance during the test campaign. To minimize wall interference effects, the entire assembly was centered within the test chamber. Given the upward-facing flow, dedicated fairings were designed in CAD and 3D-printed to streamline exposed surfaces and reduce flow separation. These fairings smoothed the transition between the nacelle and its support arm, while a beveled leading edge was added to the support bar to reduce flow disturbances caused by abrupt geometric discontinuities. The propeller setup in the test section of the wind tunnel is shown in Fig. 1.

To measure the aerodynamic loads generated by the propeller, a FUTEK MBA500 bi-axial strain gauge load cell was integrated within the internal structure of the nacelle. This sensor features a full-scale range of $\pm$222.4N for thrust and $\pm$5.65Nm for torque, with $\pm$0.25% non-linearity, and $\pm$0.05% non-repeatability. The load cell was embedded within a dedicated housing of the model, with the fixed side rigidly attached to the base support structure and the active side connected to the load transmission interface linked to the propeller hub. It was ensured that the cylindrical, non-sensitive part of the sensor did not come into contact with the surround-

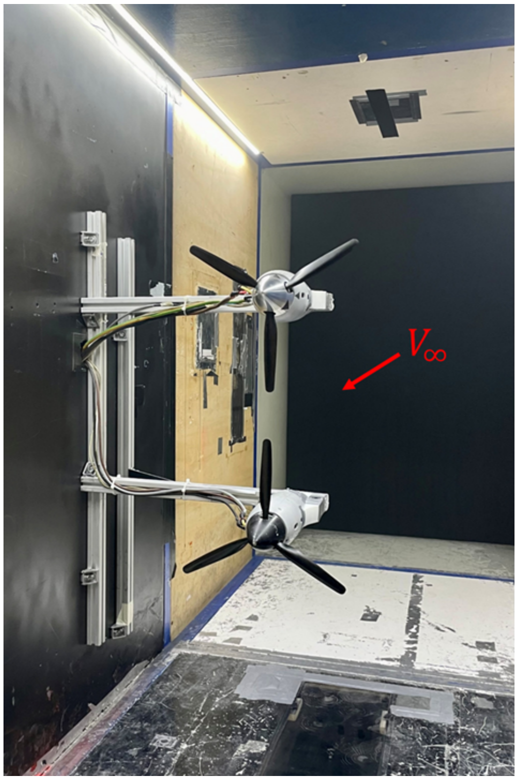

Figure 1. Layout of the VRS side-by-side propellers experimental setup at S. De Ponte wind tunnel of Politecnico di Milano.

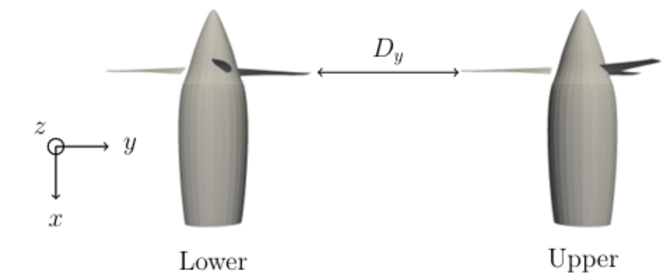

Figure 2. Layout of the propeller models with orthogonal axes

ing polycarbonate nacelle maintaining a small clearance and allowing for a free-of-interference operation. The sensor outputs were acquired using a National Instruments CompactDAQ system, equipped with a NI-9237 strain/bridge input module. Data acquisition was performed at a sampling rate of 25 kHz and for each operating point four acquisition runs were recorded to ensure the repeatability of the results and reduce the influence of transient effects. The acquired signals were then averaged. The acquisition and control procedures were managed through a custom-developed LabVIEW software environment. This setup allowed for real-time monitoring of both the propeller loads and the wind tunnel parameters, including dynamic pressure, air temperature and atmospheric pressure. A schematic layout of the two propellers is shown in Fig. 2. The orientation of the reference axes adopted as a convention throughout this work is highlighted in the scheme, as well as the distance between the propellers in the y-direction, D_y, which will be used as control parameter. In this work, D_y is defined as the lateral tip-to-tip distance between the propellers along the y-axis and is expressed as a fraction of the propeller radius. The lower propeller is taken as the reference, while the upper propeller is displaced in order to vary the distance D_y.

The test matrix is reported in Tab. 1. For each configuration, the wind tunnel speed was systematically varied, covering descent ratios from 0 up to approximately 2, while keeping fixed to 7000 RPM the rotational speed of both propellers. For each test, the wind tunnel speed was manually adjusted to achieve the correct descent ratio relative to the velocity measured downstream of the tunnel's contraction section. This procedure was necessary due to the induced velocity generated by the propellers in the opposite direction.

Configuration	D_y	Rotation Sense	Descent Ratios [-]
Single	–	–	0 - 2
Tandem	1R	Co-rotating	0 - 2
Tandem	0.5R	Co-rotating	0 - 2
Tandem	0.3R	Co-rotating	0 - 2
Tandem	0.1R	Co-rotating	0 - 2
Tandem	0.1R	Counter-rotating	0 - 2

Table 1. Load measurements test matrix with different rotor configurations and descent ratio

Given the importance of hover thrust value, which was used as a reference in performance metrics and comparisons, an independent additional measurement campaign was performed outside the wind tunnel test section allowing the acquisition of unconfined thrust data free from wall interference effects.

Two-dimensional PIV surveys were employed to characterize the flow field generated by the propeller dual-system. The experimental arrangement included a dual-head Nd:YAG Quantel Evergreen laser ($\lambda = 532$nm, 200mJ per pulse), positioned beneath the transparent floor of the wind tunnel. A 90° optical mirror was employed to redirect the laser beam upward, forming a planar light sheet approximately with the longitudinal plane of the model for flow field illumination. Due to mechanical constraints related to the placement of the calibration target, the light sheet was positioned 5.8 cm offset from the exact mid-span between the two propellers. Two ILA.PIV.sCMOS cameras (16-bit, 2560 x 2160 pixels) were installed outside the test section in a vertical tandem configuration. This configuration allowed for the acquisition of two distinct but slightly overlapping image windows, which were merged through interpolation during post-processing, thus capturing the wake of the lower propeller and, depending on the spacing configuration, part of the upper propeller as well. The cameras were rigidly mounted on an external frame to ensure proper alignment and to minimize vibrations. A slight overlap between the camera fields of view enabled reconstruction of a continuous measurement plane. Flow seeding was performed using a PIVTEC PIVpart30 generator equipped with Laskin nozzles, producing oil-based tracer particles with diameters in the range of $1-2\mu$m. This ensured effective light scattering and accurate flow tracking. Figure 3 shows both the calibration target in the test section and the cameras setup.

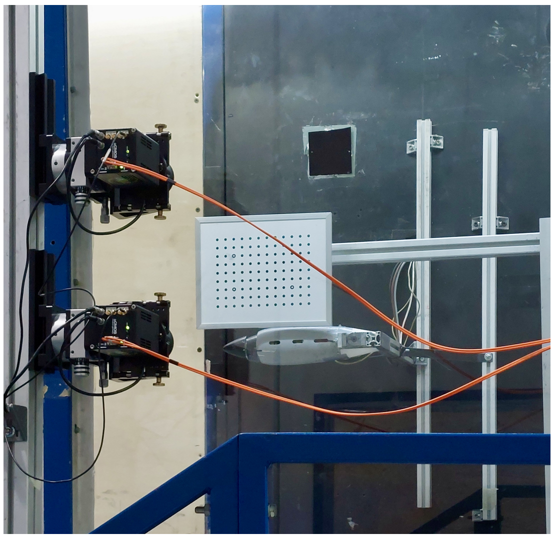

Figure 3. PIV calibration target and cameras setup in the test section.

Free-run acquisition over 500 double-frame image pairs were collected for each test configuration. PIV image analysis was performed using PIVview 3C software (PIVTEC GmbH). A multi-pass, multi-grid cross-correlation algorithm was applied, with interrogation windows starting from 128 x 128 pixels to 32 x 32 pixels. Regions obscured by the nacelle or propeller blades were masked prior to processing. To effectively characterize the descent condition and investigate the onset and development of the Vortex Ring State, four increasing descent ratios among the ones considered in the test matrix were investigated for each propeller configuration tested. These freestream velocities were selected to span from near-hover conditions to descent regimes with increasing severity, allowing the progressive transition into and out of the VRS to be captured.

RESULTS AND DISCUSSION

Loads Measurement

For the discussion of thrust measurements the lower propeller was used as the primary reference in the tandem configuration, allowing for a consistent comparison of thrust and torque behavior with respect to single propeller configuration. Nevertheless, a preliminary analysis of the loads measured on the upper propeller confirms the symmetrical behaviour of the tandem setup.

Figure 4 compares the thrust (C_T) and torque (C_Q) coefficients as function of the descent ratio (DR) measured for the single and the lower propeller in tandem for all the lateral separation distances tested.

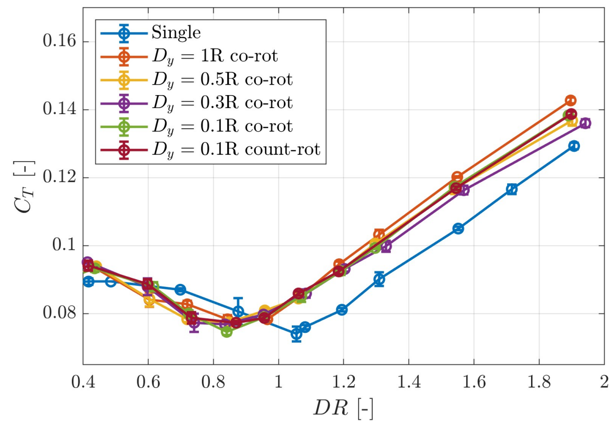

(a)

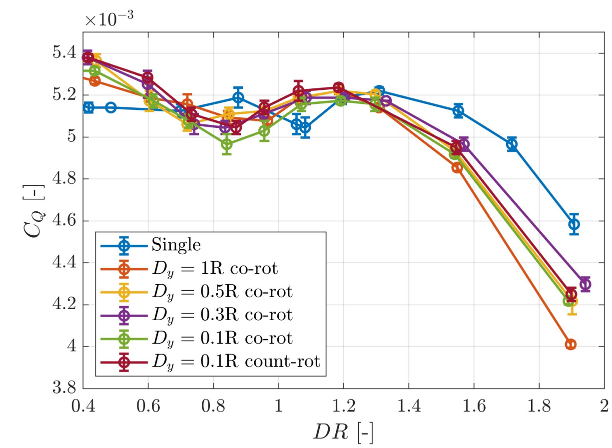

(b)

Figure 4. Comparison of the thrust (C_T) and torque (C_Q) coefficients as function of the descent ratio (DR).

The curve comparison shows a loading drop at approximately $DR \approx 1$ for the single propeller configuration, which is consistent with the physical occurrence of VRS. As the descent ratio increases beyond this point, the propeller begins to recover part of its thrust. This behavior aligns with the known transition from VRS and turbulent-wake-state to windmill-brake or autorotation regimes, where the descent airflow becomes more stable. A similar trend can be observed in the torque coefficient curve. Around $DR \approx 1$, a noticeable drop in C_Q is also present, corresponding to the onset of VRS. However, unlike the thrust coefficient, the torque coefficient continues to decrease as the descent ratio increases beyond this point. The progressive decline in C_Q reflects the decreasing power demand of the rotor as it enters an energy-absorbing aerodynamic state.

In the tandem cases, the curves exhibit almost a horizontal shift with respect to descent ratio. The observed horizontal offset between the tandem and single propeller curves can be related to two main effects: interactional effects between the wake structures generated by the two propellers, and the higher wind tunnel interference effect, i.e. solid and wake blockages, due to the presence of the second propeller in the test section, which doubles the cross-sectional area of the system with respect to the test section. However, since the tested flight conditions fall outside the range considered by classical wall interference correction models, for instance Glauert's correction (Ref. 13), no rigorous correction on the measured loads coefficients were applied. Further investigation of this aspect is the goal of the future development of this activity, particularly by considering to test the same tandem propeller set up in a wind tunnel with a larger test section.

On the other hand, the loads coefficients curves obtained for the different tandem configurations, including variations in vertical distance and rotation sense, show small differences among each other and present a similar drop in performance comparable to the one measured for the single propeller configuration. This feature suggests that the lateral distance between the propellers and the sense of rotation do not significantly affect the propeller performance. To provide a quantitative representation of the performance losses effects, Fig. 5 shows the comparison of the percentage thrust drop with respect to hover condition occurring at descent ratio corresponding to VRS occurrence for all configurations.

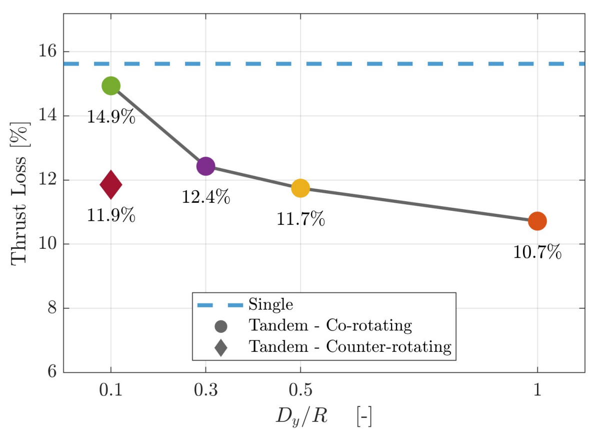

Figure 5. Comparison of percentage performance losses occurring at VRS descent ratio with respect to hover condition.

This analysis highlights how in general all tandem configurations are characterized by a lower loss of propeller thrust with respect to the single propeller case. Moreover, results shows that increasing the distance between the propellers, the thrust loss in VRS condition becomes slighlty smaller, while counter-rotating blades provides an attenuation of the performance losses at the lowest lateral separation distance between the propellers.

In addition, to gain further insight into the analysis of performance losses due to VRS occurrence, a normalized representation of the thrust coefficient with respect to the value measured in hover ($C_{T,0}$) is discussed. Indeed, when the normalized thrust coefficient $C_T/C_{T,0}$ drops below unity, the propeller is producing less thrust than in hover. The extent of this condition and the corresponding descent ratio range was considered as a meaningful indicator of VRS severity. While the area under the curve could serve as a global metric of thrust loss, it is sensitive to the interpolation scheme due to the relatively sparse experimental data points. To maintain robustness and avoid overfitting, a linear interpolation was used between the experimental data points, offering a conservative yet reliable representation of the trend. Figure 6 illustrates the normalized thrust coefficients curves, focused on the segments where $C_T/C_{T,0} < 1$. This approach allows for a clearer visual comparison of the operational descent ratio range in which thrust degradation occurs.

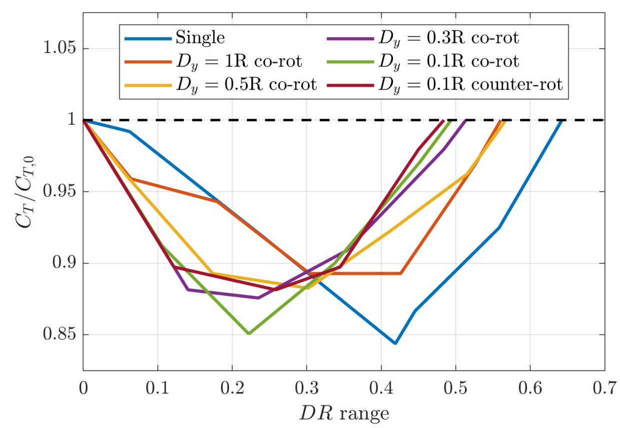

Figure 6. Loss regions comparison

It is clear that the single propeller configuration exhibits the widest loss region, both in terms of thrust magnitude and descent ratio span. Interestingly, a qualitative trend emerges by analysing the curves obtained for the lower propeller in tandem. As the lateral distance between the propellers in tandem configurations decreases, the descent range affected by thrust degradation also becomes smaller. Additionally, the area of the loss region is consistently smaller in the tandem configurations than in the single-propeller case, suggesting a mitigation effect induced by the tandem arrangement. These results supports the hypothesis that the tandem configuration attenuates the detrimental impact of VRS, both in terms of maximum thrust loss, duration of the degraded performance and overall integrated effect. This hypothesis will be supported by the discussion of PIV results in the next section. Furthermore, no significant differences were observed between the co-rotating and counter-rotating configurations at equal lowest lateral spacing, indicating that rotational direction has a negligible influence on the global performance behavior under descent.

Particle Image Velocimetry

PIV measurements were performed for all configurations under investigation, at four different descent ratios. For each propeller configuration, the averaged PIV fields are shows by the axial velocity component (V_x) contours and in-plane streamlines.

The first analysis, whose results are shown in Fig. 7 focuses on the single propeller configuration, used as a reference to investigate the general behavior of the vortex ring without interference from a second propeller. As the descend speed increases, a recirculation region gradually forms from below the propeller disk, eventually organizing at DR = 1.1 into a clear vortex ring structure that then moves upwards, in agreement with the known progression of VRS generation.

Expanding the analysis to tandem propeller configurations allows for the investigation of the interactions between the vortex rings generated by the two propellers. Fig. 8 presents the results for a tip-to-tip distance of D_y = 1R, where two clearly separated and symmetric vortex rings are formed. The symmetry of the setup is well preserved and no significant deformation of the vortical structures is observed.

Figure 9 shows the flow fields corresponding to tandem propellers at $D_y = 0.5$R. As the distance between the propellers is reduced, the inner vortices begin to interact. Despite evident deformation and compression, two distinct vortex structures remain clearly detectable, although with a visibly reduced core radius. As the descent ratio increases, the evolution of the vortex structures follows the behaviour previously observed, characterized by displacement from the rotor disk plane and radial expansion, ultimately leading to dissipation.

A further reduction in the inter-rotor lateral spacing leads to enhanced vortex ring interaction, deformation and eventual merging. At $D_y = 0.3$R, whose flow fields are shown in Fig.10, the characteristic dual-vortex structure between the propellers is no longer observed at $DR = 0.9$.

This phenomenon becomes more pronounced at at $D_y = 0.1$R, as illustrated in Fig. 11, where the lack of inter-propeller vortical structures suggests the formation of a single, unified vortex ring enclosing both rotors. Interestingly, once the VRS condition is exceeded with increasing descent ratio, two separate and independent vortical structures reappear for each propeller, detaching from their respective propeller disk planes and propagating downstream. It can be observed that the formation of inner vortices, and consequently the breakdown of a single, unified vortex ring generated by both propellers, occurs at progressively higher descent ratios as the distance between the propellers decreases. This phenomenon is consistent with the differences in the load curves discussed in the previous section.

The analysis of the counter-rotating configuration, presented in Fig. 12, indicates that at same lowest lateral distance between the propellers $D_y = 0.1$R but with opposite rotational directions, the overall flow field topology remains fundamentally unaltered. This observation suggests that the direction of rotation has a negligible effect on the overall flow characteristics and the large-scale vortex structure, as also indicated by the load curves shown in the previous section.

Figure 13 allows for a comparative analysis of the different configurations at $DR = 0.9$, the condition closest to VRS occurrence in the tandem configurations, providing valuable insights. Starting from the $D_y = 1$R case, the flow field topology closely resembles that of two isolated rotors. As the inter-rotor spacing decreases, interaction between the inner vortices becomes apparent. Indeed, at $D_y = 0.5$R the inner vortices appear compressed and reduced in size, while still maintaining a distinct structure and coherence. Further reduction in lateral spacing leads to the progressive coalescence of the inner vortices, culminating in complete merging at $D_y = 0.1$R. Additionally, comparison with the counter-rotating configuration supports that rotational direction produces negligible differences in the observed flow field characteristics.

Building upon the valuable insights provided by flow field visualizations, it is possible to deepen the analysis by seeking quantitative information to achieve a more comprehensive understanding of the phenomenon. A particularly valuable tool in this study is the identification of the vortex core positions. Specifically, the vortex center was determined using an approach based on the identification of the vortex location by tracing in-plane streamlines from the PIV-averaged flow fields. When streamlines twist or close around a circular structure, they provide a clear identification of the vortex core. In particular, the center of curvature method was used in the present work, as described in details in (Ref. 14). Indeed, in vortical regions of the flow field, the centers of curvature of several nearly circular streamlines accumulate at a point, that is considered the vortex center position. This method was applied to the averaged flow fields to provide a comprehensive understanding of the vortex ring evolution around the propeller by analysing the trajectories of the vortex core centers along the entire range of descent ratios for all tested conditions.

Figure 14 compares the vortex center trajectories for all configurations. The upward displacement of the vortex center with increasing descent ratio is consistently observed across all configurations. While the general trend of upward movement is similar regardless of inter-propeller spacing, it is interesting to observe that the vortex center positions at $DR = 0.9$, marked with diamond symbols, align closely across all tandem cases. In contrast, for the single propeller configuration, both the vortex center location and the streamline pattern indicate a pre-VRS condition, with the onset of VRS occurring closer to $DR = 1.1$. This observation is consistent with the C_T and C_Q curves shown earlier in Fig. 4, which highlight a shift in the lowest load peak corresponding to VRS onset between the single and tandem configurations, thus resembling an earlier VRS onset for the tandem case.

Once the vortex center positions had been identified, the analysis was further extended by computing the tangential ve-

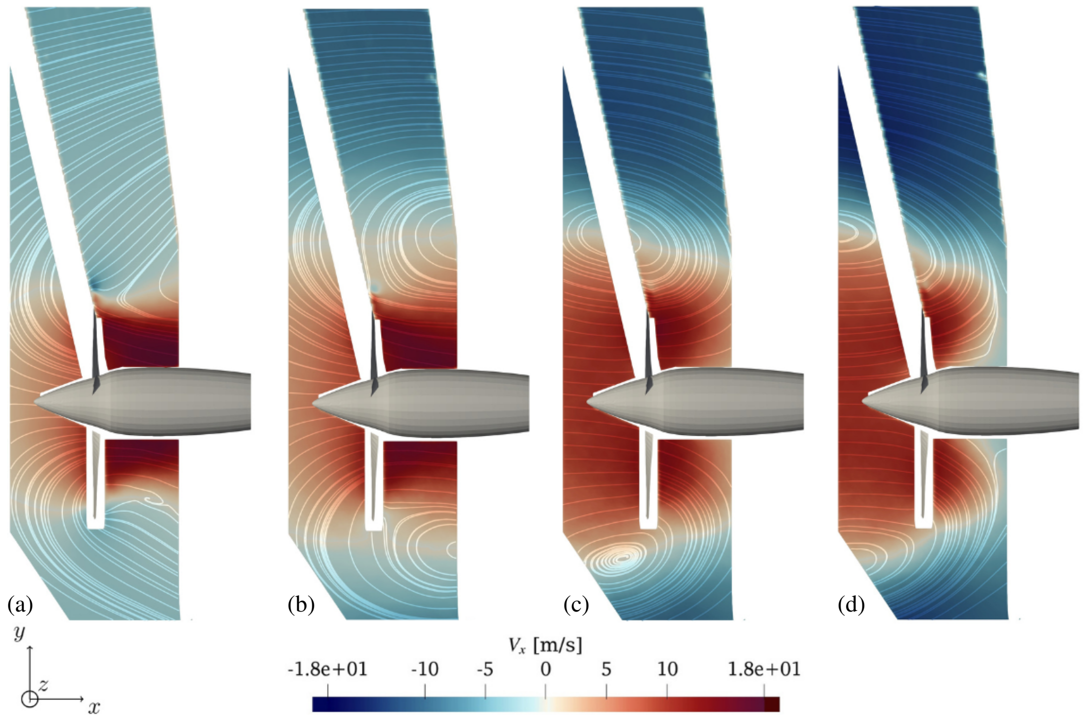

Figure 7. Comparison of the PIV averaged axial velocity component flow field for single propeller configuration,(a) $DR = 0.5$**, (b)** $DR = 0.9$**, (c)** $DR = 1.1$ **and (d)** $DR = 1.3$

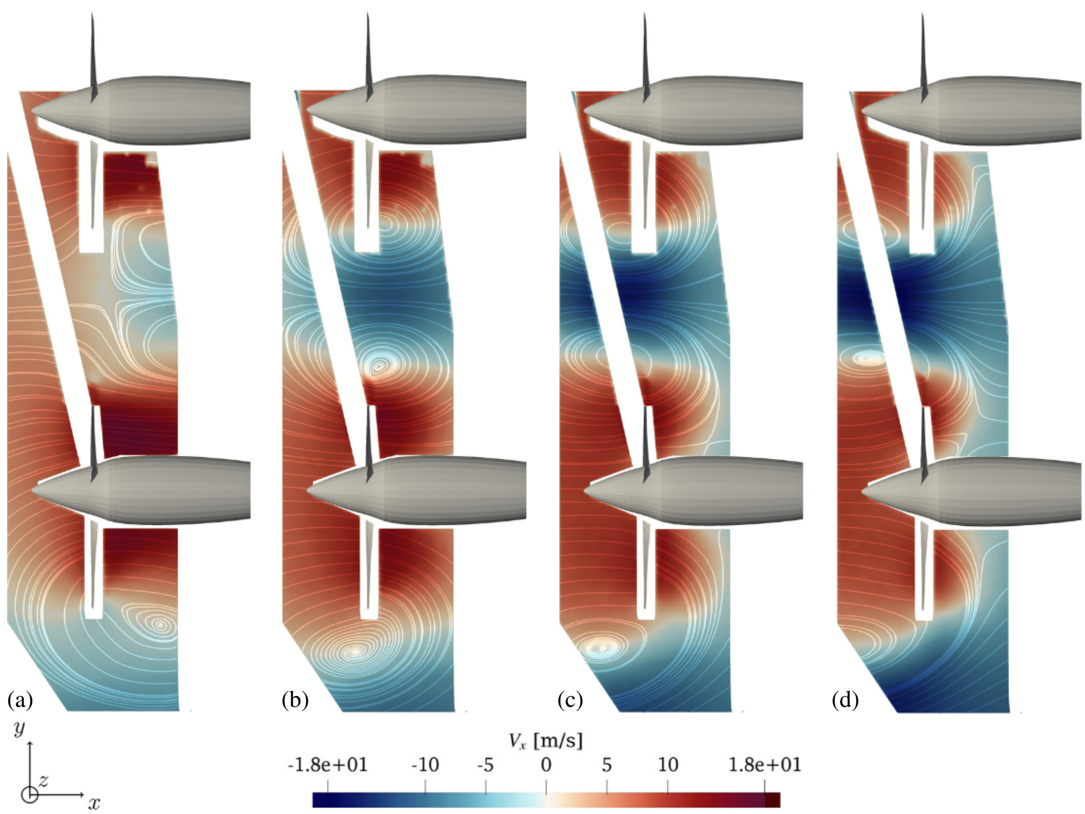

Figure 8. Comparison of the PIV averaged axial velocity component flow field for tandem co-rotating propeller configuration with $D_y = 1\text{R}$**, (a)** $DR = 0.7$**, (b)** $DR = 0.9$**, (c)** $DR = 1.1$ **and (d)** $DR = 1.3$

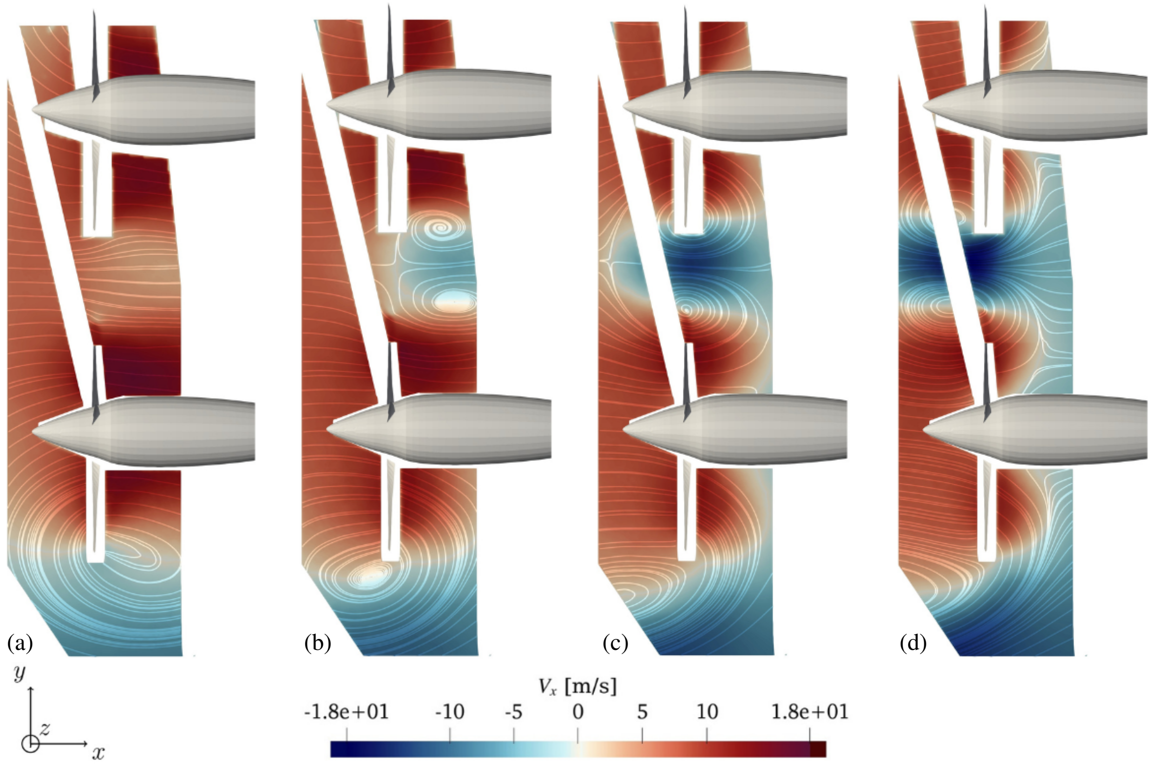

Figure 9. Comparison of the PIV averaged axial velocity component flow field for tandem co-rotating propeller configuration with $D_y = 0.5$R, (a) $DR = 0.7$, (b) $DR = 0.9$, (c) $DR = 1.1$ and (d) $DR = 1.3$

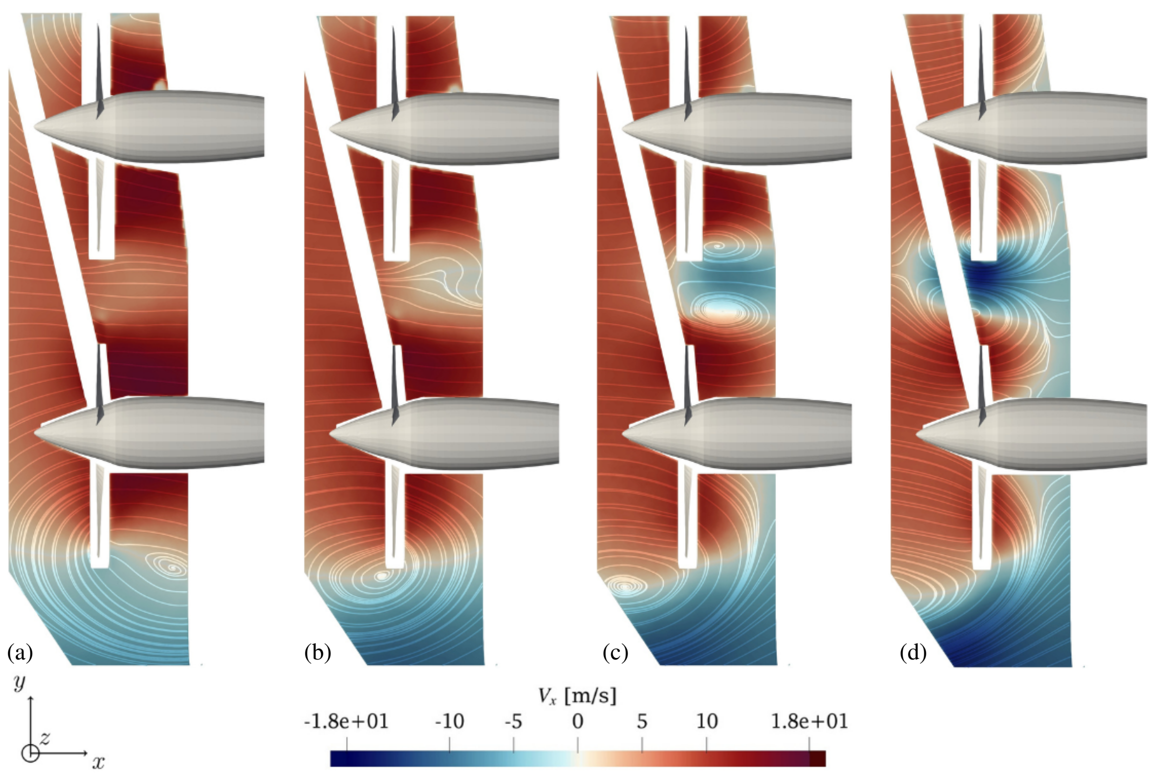

Figure 10. Comparison of the PIV averaged axial velocity component flow field for tandem co-rotating propeller configuration with $D_y = 0.3$R, (a) $DR = 0.7$, (b) $DR = 0.9$, (c) $DR = 1.1$ and (d) $DR = 1.3$

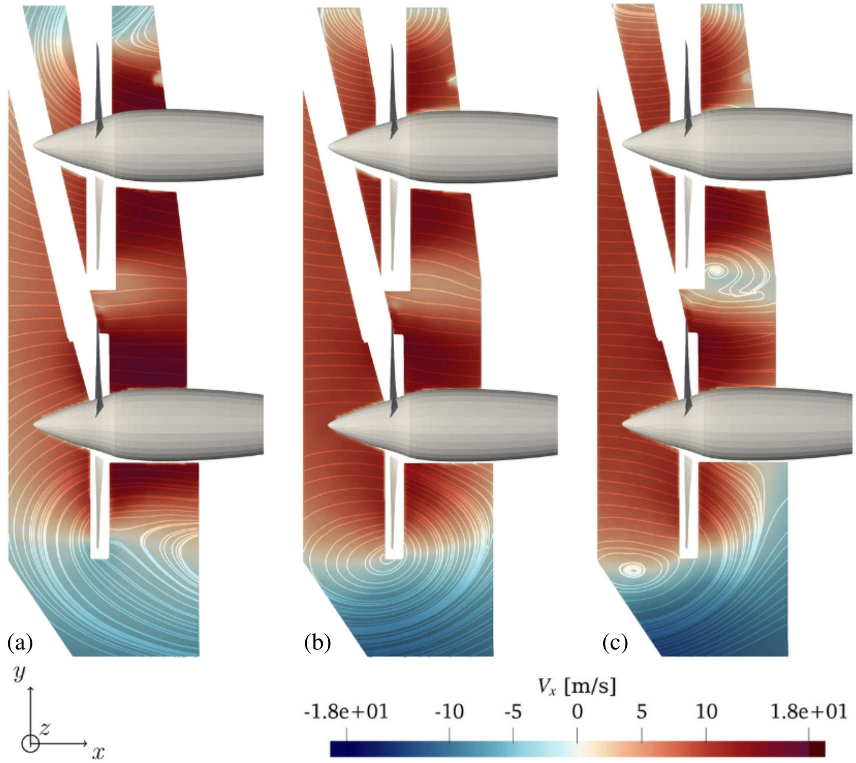

Figure 11. Comparison of the PIV averaged axial velocity component flow field for tandem co-rotating propeller configuration with $D_y = 0.1\mathrm{R}$, (a) $DR = 0.7$, (b) $DR = 0.9$, (c) $DR = 1.1$ and (d) $DR = 1.3$

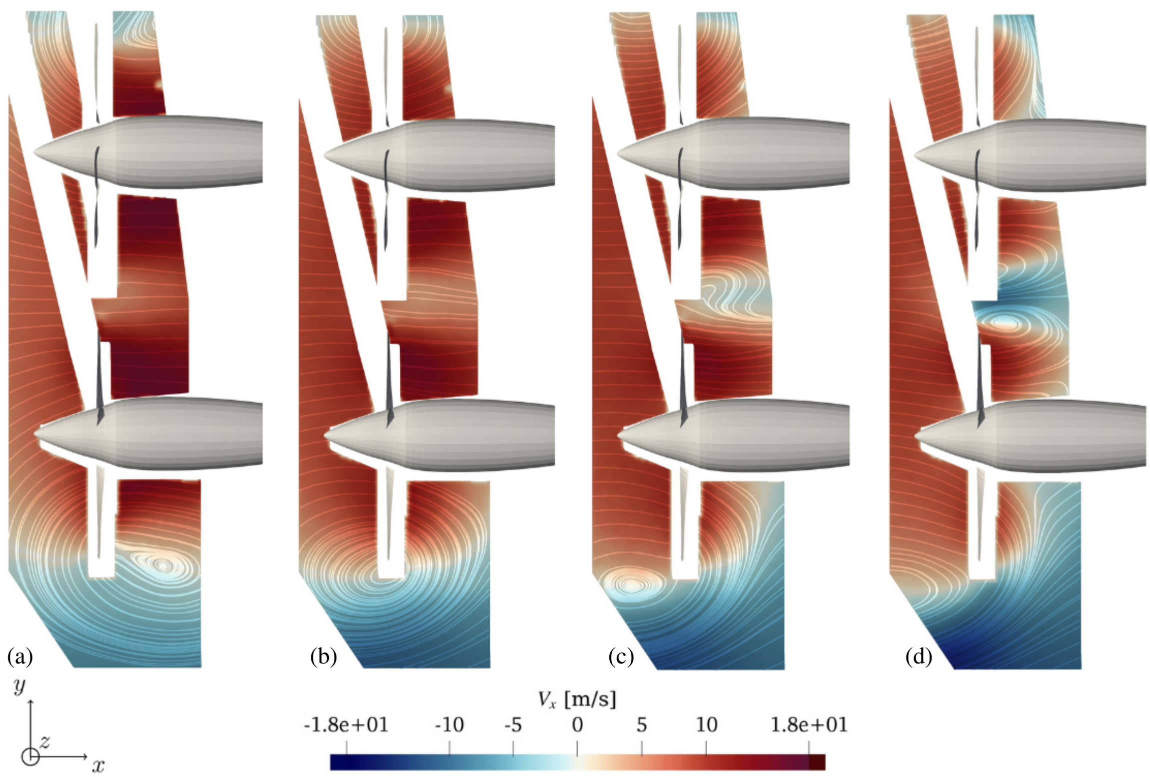

Figure 12. Comparison of the PIV averaged axial velocity component flow field for tandem counter-rotating propeller configuration with $D_y = 0.1\mathrm{R}$, (a) $DR = 0.7$, (b) $DR = 0.9$, (c) $DR = 1.1$ and (d) $DR = 1.3$

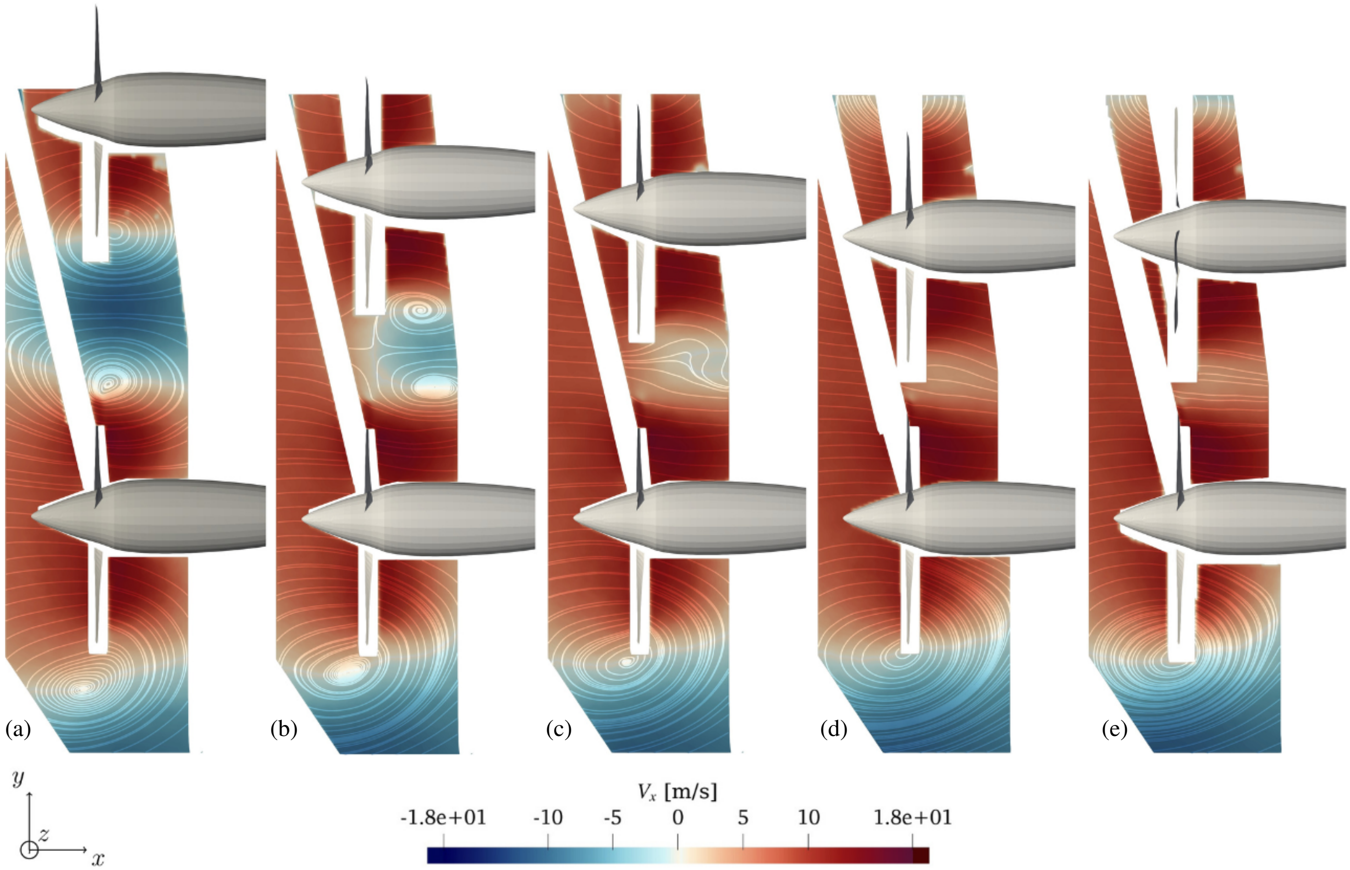

Figure 13. Comparison of the PIV averaged axial velocity component flow field for tandem propeller configuration at $DR = 0.9$**, (a)** $D_y = 1\mathrm{R}$**, (b)** $D_y = 0.5\mathrm{R}$**, (c)** $D_y = 0.3\mathrm{R}$**, (d)** $D_y = 0.1\mathrm{R}$ **and (e)** $D_y = 0.1\mathrm{R}$ **counter-rotating**

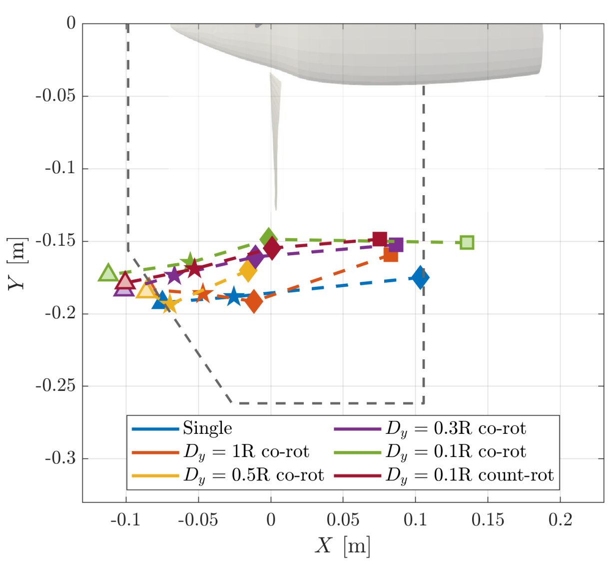

Figure 14. Comparison between all configurations of the lower propeller's outer vortex tracking for increasing descent ratio

locity within the flow field, with the aim of determining the vortex core radii. The vortex core radius can be then determined as the radial distance from the vortex center to where the angle-averaged tangential velocity, calculated on the area of investigation, reaches its maximum value, as done in Gibertini et al. (Ref. 15). This method was applied to all tested configurations for the detection of both inner and outer vortices radii. Figure 15 compares the vortex radii, displaying their normalized values as a function of the inter-rotor spacing, with respect to the single propeller baseline.

It is noteworthy that the vortex radii are smaller than the single propeller reference case for inter-rotor distances of $D_y = 0.3\mathrm{R}$ and $D_y = 0.5\mathrm{R}$, while they remain approximately aligned with the single propeller case at $D_y = 0.1\mathrm{R}$ and $D_y = 1\mathrm{R}$. Moreover, the agreement between the inner and outer vortex radii in the single-propeller configuration confirms the expected symmetry of the flow structure, while a significant difference in the inner vortex radii is observed between the $D_y = 1\mathrm{R}$ and $D_y = 0.5\mathrm{R}$ tandem configurations. This discrepancy may partially account for a more substantial thrust loss experienced by the single propeller compared to the tandem configurations. Interestingly, the variation in vortex radius appears to correlate with the trend in thrust loss percentage shown in Fig. 5, with the exception of the $D_y = 1\mathrm{R}$ case.

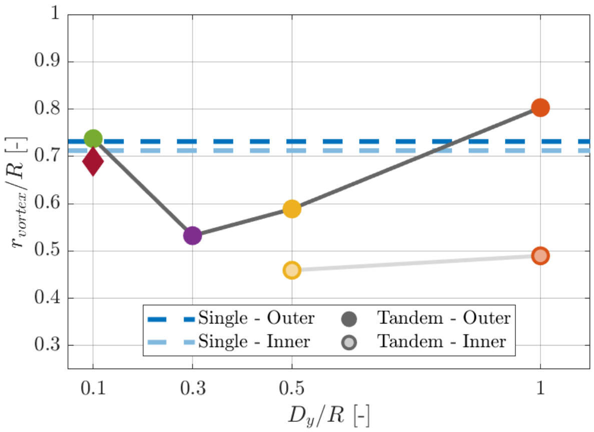

Figure 15. Comparison of the normalized radius of both the outer and inner vortices, as a function of inter-rotor distance D_y for all configurations, with respect to the single configuration

CONCLUSIONS

A comprehensive experimental campaign was performed to investigate vortex ring state for a tandem propeller configurations with variable lateral distance. Wind tunnel tests enabled to evaluate the effects of aerodynamics interactions typical or multiple-rotor eVTOL configurations on the occurrence of VRS phenomenon in descent flight conditions. Loads measurements showed a similar amount of performance drop in VRS condition between single and tandem propeller configurations, but occurring at an earlier descent ration for the tandem case. In particular this latter performance drop does not sensibly change while diminuishig the lateral distance between propeller disks. PIV surveys enabled to fully characterise the flow physics related to the phenomenon. In particular, while diminuishing the lateral distance between the tandem propellers, the inner vortices reduced their dimensions due to their mutual interaction until they coalesce. Moreover, the flow fields confirms that in tandem configuration, the generation of a large vortex structure typical of VRS occurs in the region of the propeller disk at an earlier descent ratio with respect to single propeller configuration. Future development of the present activity will be dedicated to investigate the cause of this latter effect observed for the tandem propeller configurations in order to quantify if this effect is due to the mutual interaction between the propeller wakes or to an increase of the blockage effect in the wind tunnel.

Authors contact:
Caterina Saglio caterina.saglio@mail.polimi.it
Daniele Granata daniele.granata@polimi.it
Alberto savino alberto.savino@polimi.it
Alex Zanotti alex.zanotti@polimi.it

REFERENCES

1. Leishman, G. J., *Principles of helicopter aerodynamics*, Cambridge university press, 2006.
2. Johnson, W., *Rotorcraft Aeromechanics*, Cambridge Aerospace Series, Cambridge University Press, Cambridge, electronic resource edition, 2013. DOI: 10.1017/CBO9781139235655.
3. Betzina, M. D., "Tiltrotor descent aerodynamics: A small-scale experimental investigation of vortex ring state," American Helicopter Society 57th Annual Forum, Washington, DC, 2001.
4. Brand, A., Kisor, R., Blyth, R., Mason, D., and Host, C., "V-22 high rate of descent (hrod) test procedures and long record analysis," American helicopter society 60th annual forum, Baltimore, MD, 2004.
5. Stack, J., "Experimental investigation of rotor vortex wakes in descent," 42nd AIAA Aerospace Sciences Meeting and Exhibit, 2004.
6. Shetty, O., and Selig, M., "Small-scale propellers operating in the vortex ring state," 49th AIAA Aerospace Sciences Meeting including the New Horizons Forum and Aerospace Exposition, 2011.
7. Brown, R. E., "Are eVTOL aircraft inherently more susceptible to the vortex ring state than conventional helicopters?" 48th European Rotorcraft Forum, 2022.
8. Jeong, T., Hong, Y., and Yee, K., "Extension of the Analytic Vortex Ring State Model for eVTOL Application," , 2024.
9. Savino, A., Gianotti, A., Droandi, G., Kerho, M., and Zanotti, A., "Experimental investigation of vortex ring state in an eVTOL propeller," *Aerospace Science and Technology*, Vol. 165, 2025, pp. 110475. DOI: https://doi.org/10.1016/j.ast.2025.110475.
10. Zagaglia et al., D., "Experimental investigation into the vortex ring state of multi-rotor configurations," 50th European Rotorcraft Forum, 2024.
11. Granata, D., Savino, A., Grassi, D., Riccobene, L., and Zanotti, A., "Aerodynamic and aeroacoustics investigation of tandem propellers in hover for eVTOL configurations," *Aerospace Science and Technology*, Vol. 155, 2024, pp. 109740.
12. Zanotti, A., and Algarotti, D., "Aerodynamic interaction between tandem overlapping propellers in eVTOL airplane mode flight condition," *Aerospace Science and Technology*, Vol. 124, 2022, pp. 107518. DOI: https://doi.org/10.1016/j.ast.2022.107518.
13. Glauert, H., "The analysis of experimental results in the windmill brake and vortex ring states of an airscrew, r & m no. 1026," *British ARC*, 1926.

14. Ari Sadarjoen, I., and Post, F. H., "Detection, quantification, and tracking of vortices using streamline geometry," *Computers & Graphics*, Vol. 24, (3), 2000, pp. 333–341. DOI: https://doi.org/10.1016/S0097-8493(00)00029-7.

15. Gibertini, G., Mencarelli, A., and Zanotti, A., "Oscillating aerofoil and perpendicular vortex interaction," *Proceedings of the Institution of Mechanical Engineers, Part G: Journal of Aerospace Engineering*, Vol. 228, (6), 2014, pp. 846–858. DOI: 10.1177/0954410013481154.

CLASSIFICATION & COPYRIGHT